

ARTICLE

Open Access

# Unique phonon modes of a $\text{CH}_3\text{NH}_3\text{PbBr}_3$ hybrid perovskite film without the influence of defect structures: an attempt toward a novel THz-based application

Inhee Maeng<sup>1</sup>, Seungjun Lee<sup>2</sup>, Hiroshi Tanaka<sup>3</sup>, Jung-Ho Yun<sup>4</sup>, Shenghao Wang<sup>5</sup>, Masakazu Nakamura<sup>3</sup>, Young-Kyun Kwon<sup>2</sup> and Min-Cherl Jung<sup>6</sup>

## Abstract

The exploration of new physical properties for various THz-based applications, such as THz-wave sensing, modulation, and imaging devices, is a key challenge in the research on organic–inorganic hybrid perovskite materials. These THz-based applications require satisfactory, sensitive, and stable absorption properties with values between 0.5 and 3 THz. To achieve these properties, candidate materials should possess a purified structure that induces regular and fixed phonon modes without any defects or impurities.  $\text{CH}_3\text{NH}_3\text{PbBr}_3$ , an organic–inorganic hybrid perovskite thin film produced by a sequential vacuum evaporation method on a flexible PET substrate, was investigated in this study. Although the thin film contains only molecular defects related to  $\text{CH}_3\text{NH}_2$  incorporated into the perovskite structure, our THz-wave absorption measurement and first-principles simulation confirmed that these molecular defects do not influence the three phonon modes originating from the transverse vibration (0.8 THz), the longitudinal optical vibrations (1.4 THz) of the Pb–Br–Pb bonds, and the optical Br vibration (2.0 THz). After spin-casting an ultrathin PTAA polymer protective layer (5 nm) on the hybrid perovskite thin film, it was additionally observed that there was no significant effect on the phonon modes. Thus, this novel flexible organic–inorganic hybrid perovskite material is a potential candidate for THz-based applications.

## Introduction

Recently, organic–inorganic hybrid perovskite (OHP) materials have been used in several applications, such as solar cells, light-emitting diodes, lasers, and memory devices<sup>1–5</sup>. In the last decade, OHP materials have shown excellent results, especially in the case of solar cells, including a power conversion efficiency of over 25%, because of their key physical properties, such as a high absorption coefficient, high carrier mobility, and long

carrier lifetime<sup>6–9</sup>. Moreover, the solution-based fabrication method for thin films is highly compatible with the current industrial requirements of easy fabrication processes and low unit costs<sup>10–12</sup>. However, attempts to improve the main requirements of material stability and a Pb-free nature have continued because research on OHP materials is still focused on solar cell applications<sup>13–19</sup>.

The exploration of new physical properties for novel device applications requires a deep understanding of the fundamental physical properties, such as the defects, phonon-dispersion relations, and electronic structures. This understanding enables the explanation of and provides the solution for several unexpected behaviors observed in OHP-based devices, such as material instability, migration of halogen anions, short lifetime in

Correspondence: Young-Kyun Kwon (ykkwon@khu.ac.kr) or Min-Cherl Jung (jung.mincherl.fp@utsukuba.ac.jp)

<sup>1</sup>YUHS-KRIBB, Medical Convergence Research Institute, College of Medicine, Yonsei University, Seoul 03722, Republic of Korea

<sup>2</sup>Department of Physics, Kyung Hee University, Seoul 02447, Republic of Korea  
Full list of author information is available at the end of the article

These authors contributed equally: Inhee Maeng, Seungjun Lee, Hiroshi Tanaka

© The Author(s) 2020



**Open Access** This article is licensed under a Creative Commons Attribution 4.0 International License, which permits use, sharing, adaptation, distribution and reproduction in any medium or format, as long as you give appropriate credit to the original author(s) and the source, provide a link to the Creative Commons license, and indicate if changes were made. The images or other third party material in this article are included in the article's Creative Commons license, unless indicated otherwise in a credit line to the material. If material is not included in the article's Creative Commons license and your intended use is not permitted by statutory regulation or exceeds the permitted use, you will need to obtain permission directly from the copyright holder. To view a copy of this license, visit <http://creativecommons.org/licenses/by/4.0/>.

devices, and the bandgap distribution<sup>17,20–23</sup>. Although numerous new physical properties of OHP materials have been discovered that have led to improvements in device performance, the phonon-related behavior of these materials, especially in the THz energy range (0.5–3 THz), is yet to be fully understood<sup>24,25</sup>.

According to previous literature, OHP materials possess both molecular vibrations from the organic portion as well as lattice vibrations from the inorganic portion because of the lack of chemical bonding between the organic and inorganic parts<sup>4</sup>. An early study performed using powder neutron diffraction showed that the motion of the  $\text{CH}_3\text{NH}_3^+$  ( $\text{MA}^+$ ) ion was ordered, and the 2D and 3D disorder was dependent on each structure being controlled by temperature<sup>26</sup>. However, it was not possible to experimentally observe the molecular vibration and rotation in  $\text{CH}_3\text{NH}_3\text{PbI}_3$  ( $\text{MAPbI}_3$ ) and  $\alpha\text{-HC}(\text{NH}_2)_2\text{PbI}_3$  ( $\alpha\text{-FAPbI}_3$ ) thin films<sup>24,25</sup>. In the case of  $\text{MAPbI}_3$  thin films formed by a typical solution-based method, two vibrational modes at 1 and 2 THz were observed and were attributed to the buckling of the Pb–I–Pb angles and the Pb–I bond vibration, respectively<sup>27</sup>. A.M.A. Leguy et al. investigated the vibrational modes of  $\text{MAPbX}_3$  ( $X = \text{Cl}, \text{Br}, \text{and I}$ ) with the help of Raman spectroscopy and theoretical simulations<sup>28</sup>. Their report revealed several interesting modes in hybrid perovskite structures. The contribution of molecular motion was very weak in the THz energy range. Additionally, a high absorption with a vibration of 1.58 THz was observed for  $\text{MAPbI}_3$ , which possessed a hybrid perovskite structure incorporating the  $\text{CH}_3\text{NH}_2$  molecular defect that was produced using the sequential vacuum evaporation (SVE) method<sup>25,29</sup>. Moreover,  $\alpha\text{-FAPbI}_3$  thin films fabricated by the SVE method showed an absorption of 1.62 THz<sup>24</sup>. Recent reports imply that a vacuum-processed method such as the SVE method can create a greater number of variable states than a solution-processed method because vacuum-processed methods produce smaller grains and a high density of grain boundaries and defects<sup>24,25,29</sup>. Hence, it is crucial to focus on vacuum-processed methods to understand the variable phonon modes.

The discovery of a significant THz-wave absorption property in OHP thin films and the understanding of phonon modes will enable the use of these materials in new applications such as THz-wave sensing, modulation, and imaging devices. This is especially significant for the production of a simple transistor for THz-wave sensing devices using an OHP material that is less expensive and easier to fabricate than that produced using current materials such as highly purified GaAs<sup>30–34</sup>. In our previous work, we showed that a flexible substrate such as polyethylene terephthalate (PET) or polyestersulfone (PES) can be successfully used for THz-based applications<sup>25</sup>. In short, if we can control the THz-wave

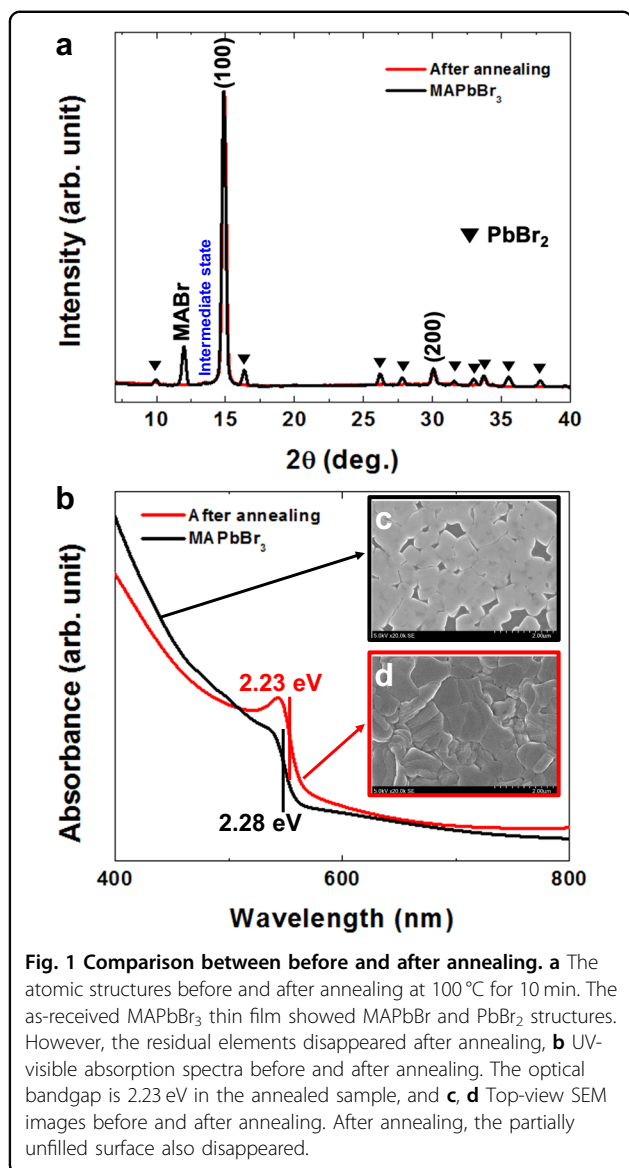
absorption property (i.e., its phonon modes) in an OHP thin film on a flexible substrate, we can eventually achieve flexible THz-wave sensing, modulation, and imaging devices.

Hence, in this study, we investigated a  $\text{CH}_3\text{NH}_3\text{PbBr}_3$  ( $\text{MAPbBr}_3$ ) hybrid perovskite thin film fabricated by the SVE method. Advanced characterization was performed to explore the atomic structures, bandgaps, surface morphologies, chemical states, and THz-wave absorption properties of the  $\text{MAPbBr}_3$  thin films. We assembled these thin films with two additional materials, namely, a PET flexible substrate and an ultrathin ( $\sim 5$  nm) [poly[bis(4-phenyl)(2,4,6-trimethylphenyl)amine]] (PTAA) polymer layer for protection. Although  $\text{CH}_3\text{NH}_2$  molecular defects and surface Pb metal defects were observed, the THz-wave absorption property of  $\text{MAPbBr}_3$  showed three regular and fixed phonon modes. In this study, we propose the possibility of a novel flexible THz-based application employing an OHP material.

## Materials and methods

$\text{MAPbBr}_3$  thin films were fabricated by the SVE method in a customized vacuum chamber<sup>25,35</sup> (S. Fig. 1, see the Supplementary Information.) A PET flexible substrate (AHCF-100, thickness = 225  $\mu\text{m}$ , AIDEN) was cleaned by sonication in acetone for 10 min, rinsed in heated acetone for 1 min, and then treated in a UV-ozone chamber for 30 min before loading it into a vacuum chamber. The base pressure of the chamber installed with a thickness sensor was  $8.0 \times 10^{-3}$  Pa. Lead(II) bromide ( $\text{PbBr}_2$ , >98% purity, Sigma-Aldrich) was evaporated at a deposition rate of 10  $\text{\AA}/\text{s}$  onto the substrates at room temperature to form a film with a thickness of 100 nm. Then, methylammonium bromide ( $\text{CH}_3\text{NH}_3\text{Br}$ , >98% purity, Sigma-Aldrich) was evaporated at a deposition rate of 2  $\text{\AA}/\text{s}$  to form a 280-nm-thick layer on the formed  $\text{PbBr}_2$  thin film to produce  $\text{MAPbBr}_3$  thin films with a thickness of 300 nm<sup>35</sup>. Further, postannealing was performed at 110  $^\circ\text{C}$  for 10 min in a  $\text{N}_2$  glovebox. Finally, spin coating was applied at 4000 rpm for 1 min to coat the resultant thin films with a PTAA (Sigma-Aldrich) solution containing 5 mg PTAA and 4 ml chlorobenzene. The PTAA solution was sonicated for 1 h.

To characterize all the formed and treated thin films, we performed X-ray diffraction (XRD), UV-visible spectrometry (V-770, JASCO), scanning electron microscopy (SEM), and high-resolution X-ray photoelectron spectroscopy. The XRD instrument was an RINT-TTRIII/NM with a Cu  $K\alpha$  source manufactured by Rigaku. The SEM equipment was a HITACHI SU9000 model, and the characterization was carried out at an acceleration voltage of 5 keV and an emission current of 10  $\mu\text{A}$ . A Versa Probe II instrument with monochromated Al  $K\alpha$  (ULVAC-PHI) was used for all XPS measurements to obtain C 1s, N 1s, Pb 4f, and I 4d core-level spectra. No



traces of O 1s core-level spectra were observed in any of the samples. The binding energies were calibrated with respect to the Au 4f<sub>7/2</sub> level (84.0 eV)<sup>36</sup>.

The THz time-domain spectroscopy (THz-TDS) spectra of the formed and treated thin films on a PET flexible substrate were measured with a standard THz-TDS transmission setup based on a Ti:sapphire regenerative amplifier system, which has 35 fs pulses at an 800 nm wavelength and a repetition rate of 1 kHz. We used a 2 mm ZnTe (110) crystal for generation and detection to measure the THz time-domain signal in the spectral range from 0.2 to 2.2 THz.

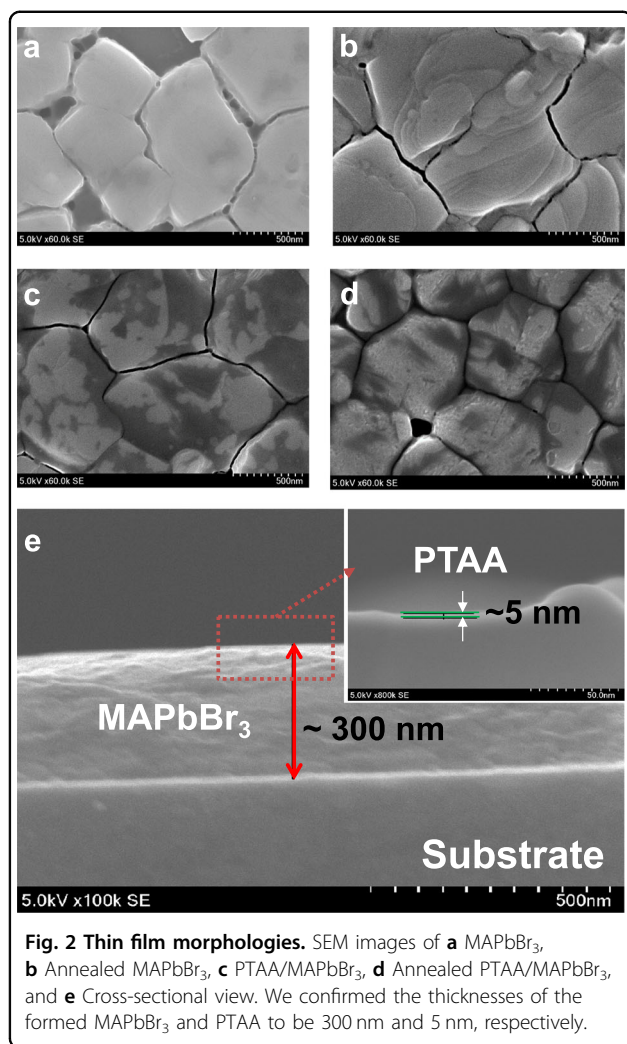
To investigate the IR absorption spectrum of MAPbBr<sub>3</sub>, we performed a first-principles calculation based on density functional theory as implemented in the Vienna ab initio simulation package (VASP)<sup>37–39</sup>. The projector-

augmented wave potentials were used to describe the valence electrons, and the exchange-correlation functional was treated with the generalized gradient approximation of Perdew–Burke–Ernzerhof with the DFT-D3 van der Waals correction<sup>40–43</sup>. The plane-wave kinetic energy cutoff was chosen to be 500 eV. The equilibrium lattice constant of cubic MAPbBr<sub>3</sub> was calculated as  $a = 5.991 \text{ \AA}$ , which agrees well with the experimental result of  $5.969 \text{ \AA}$ <sup>44</sup>. The vibrational property at finite temperatures was calculated by the temperature-dependent effective potential (TDEP) approach rather than the conventional frozen-phonon approach, since the latter approach does not well describe the finite-temperature equilibrium phases that are different from the zero-temperature phase<sup>45–47</sup>. In the TDEP approach, we performed a molecular dynamics (MD) simulation within the canonical ensemble at 300 K to compute the finite-temperature force constant matrix (FTFCM)<sup>48,49</sup>. The FTFCM was fitted by considering all the forces and displacements between any two atoms with a cutoff length of 6 Å at every time step. We used a  $2 \times 2 \times 2$  supercell structure of cubic MAPbBr<sub>3</sub> to describe the free rotation of the MA molecules as well as long-range vibrational modes. The corresponding reduced Brillouin zone was sampled only at the  $\Gamma$  point. To remove the imaginary phonon modes and to obtain the converged FTFCM, we ran the MD simulation for a total of 120,000 time steps (120 ps). We also computed the time-averaged Born effective charge (BEC) tensor, which was used with the  $\Gamma$ -point phonon eigenvectors, to obtain the IR absorption spectrum<sup>50</sup>. For comparison, we also calculated the vibrational property using the finite displacement (FD) method with the same supercell structure<sup>51</sup>.

## Results and discussion

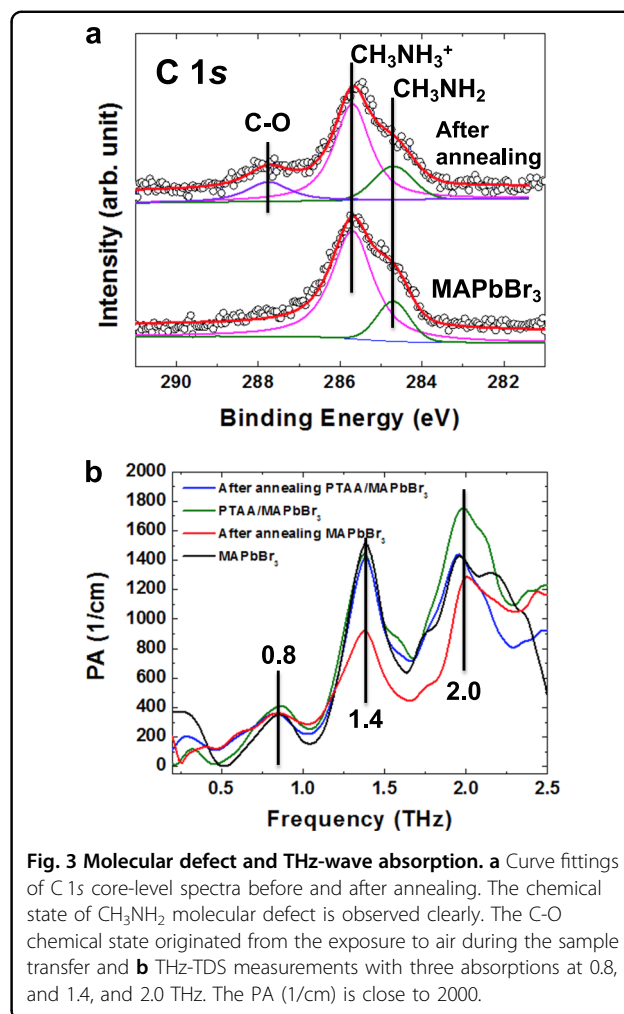
The atomic structure of MAPbBr<sub>3</sub> in Fig. 1a depicts a typical organic–inorganic hybrid perovskite structure with (100) and (200) peaks of cubic MAPbBr<sub>3</sub><sup>52</sup>. The structures of PbBr<sub>2</sub> and MABr are also observed, which disappeared after postannealing at 110 °C for 10 min. This behavior is similar to that observed in our previous research on an MAPbI<sub>3</sub> thin film<sup>53</sup>. However, unlike MAPbI<sub>3</sub>, we observed a small intermediate state, such as the CH<sub>3</sub>NH<sub>2</sub> molecular defect incorporated in the hybrid perovskite structure in MAPbBr<sub>3</sub>.<sup>24,53</sup> The MAPbBr<sub>3</sub> thin films, observed with optical bandgaps of 2.28 and 2.23 eV before and after postannealing, respectively (Fig. 1b), revealed a slight redshift in the XRD data, which is consistent with the formation of more stoichiometrically stable MAPbBr<sub>3</sub>. After annealing, the partially empty surface was filled with a step structure and a large-sized grains (Fig. 1c, d).

In the surface morphologies before and after annealing are shown in Fig. 2a–d, revealing that we found large



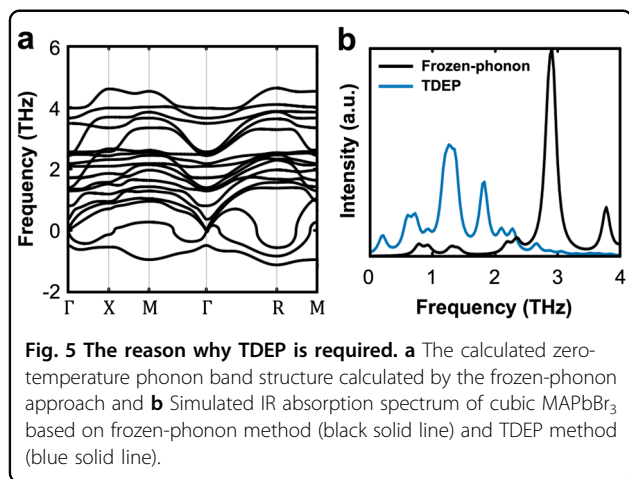
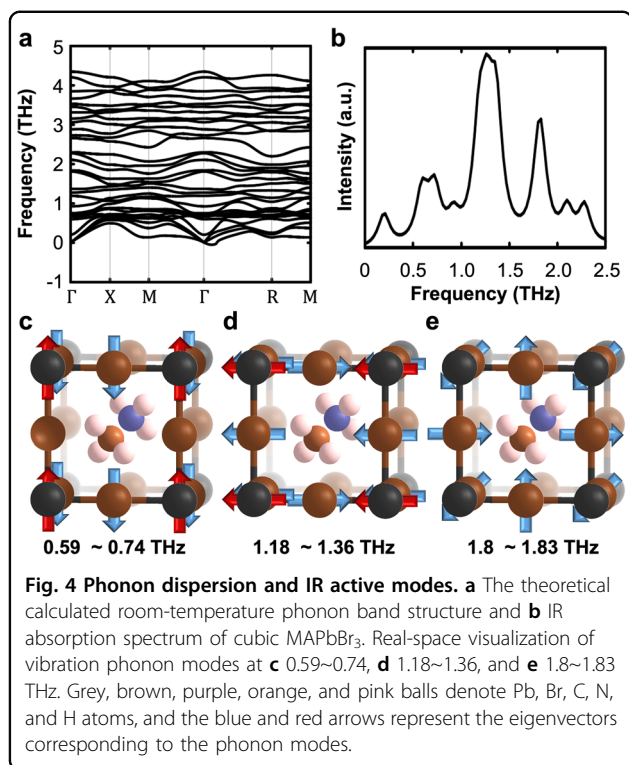
grains with a size of over 500 nm. Interestingly, the sample observed before annealing shows an unfilled surface (Fig. 2a). However, the annealed sample presents a fully filled surface composed of larger grains with clearer grain boundaries and step structures (Fig. 2b). After PTAA spin-casting, we could not observe any significant change on the film surface (Fig. 2c, d). In the cross-sectional view in Fig. 2e, the thicknesses of the MAPbBr<sub>3</sub> and PTAA layers are 300 and 5 nm, respectively.

The chemical state of the CH<sub>3</sub>NH<sub>2</sub> molecular defect was observed in the C 1s core-level spectra before and after annealing (Fig. 3a)<sup>24,53,54</sup>. The C–O bonding state in the annealed sample originated from exposure to air during sample transfer from the vacuum chamber to the N<sub>2</sub> glovebox. Interestingly, there are no new chemical states in the N 1s, Pb 4f, and Br 3d core-level spectra after annealing. This means that a small quantity of the C–O state, such as an impurity, is located only at the surface and that there is no influence on the main structure of the MAPbBr<sub>3</sub> hybrid perovskite (S. Fig. 2a–d). Surface



depletion occurs by annealing, as observed from the Pb<sup>0+</sup> chemical state (Pb metal) in the Pb 4f core-level spectrum of the annealed sample (S. Fig. 2c). However, this depletion, which induces the occurrence of the Pb metal element on the surface, does not affect the original MAPbBr<sub>3</sub> hybrid perovskite structure. After the annealing step, the intensity of the CH<sub>3</sub>NH<sub>2</sub> molecular defect decreased. Instead of the CH<sub>3</sub>NH<sub>3</sub><sup>+</sup> molecule, it is the molecular defect that is incorporated in the main hybrid perovskite structure, and it is located at the grain boundaries<sup>24</sup>. However, this structure with the defect does not appear significantly in the XRD data (Fig. 1a). This difference between MAPbI<sub>3</sub> (tetragonal) and MAPbBr<sub>3</sub> (cubic) structures may be due to their material stability, resulting from different tolerance factors<sup>55</sup>. Additionally, we confirmed the protective effect of the ultrathin PTAA layer (S. Fig. 3), from the observation that there was no change in the chemical states of MAPbBr<sub>3</sub> after exposure to air for 1 week<sup>56</sup>.

Hence, we expect that the vibrational modes of the MAPbBr<sub>3</sub> thin film with a large number of grains



originate from the main hybrid perovskite structure, such as MA (molecular vibrations), lattice vibrations (Pb–Br–Pb and independent Pb/Br vibrations), and defects, such as C–O, Pb<sup>0+</sup>, and CH<sub>3</sub>NH<sub>2</sub> molecules, included in a defect-incorporated distorted structure<sup>25,29</sup>. In the THz-wave absorption measurement using the THz-TDS system, we observed three main peaks at 0.8, 1.4, and 2.0 THz with power absorptions (PAs) of 400, 1500, and 1750 cm<sup>-1</sup>, respectively (Fig. 3b). In fact, the optical phonon modes of MAPbBr<sub>3</sub> single crystals and solution-prepared polycrystalline structures have been previously reported<sup>57,58</sup>. However, our measurement

shows the different features at room temperature, and we assume this difference is due to the SVE method, which can control the defect structures<sup>24,25,53</sup>. Additionally, we confirmed that there were no significant THz-wave absorption effects from the PTAA polymer layer and the PET flexible substrate. (Fig. 3b and S. Fig. 4) Interestingly, there is also no change in the THz-wave absorption property due to the C–O impurity, CH<sub>3</sub>NH<sub>2</sub> molecular defect, Pb metal element, and ultrathin PTAA layer. This means that the THz-wave absorption property of the MAPbBr<sub>3</sub> thin film incorporating several critical impurities and defects is fixed and stable.

To analyze the origin of the three fixed and stable THz-wave absorptions observed in our experiment, we calculated the phonon-dispersion relation and the IR absorption spectrum. Since the cubic phase of the OHP is stabilized by the rotation of organic molecules at finite temperatures, the conventional FD method provides the imaginary modes in the calculated phonon-dispersion relations. To include the molecular rotation effects in the room-temperature (RT) cubic phase of MAPbBr<sub>3</sub>, we performed a molecular dynamics simulation at 300 K and calculated the RT phonon-dispersion relation using the FTFCM described in the Methods section. Figure 4a shows the TDEP-based RT phonon-dispersion relation of cubic MAPbBr<sub>3</sub>, exhibiting no imaginary phonon modes, whereas the frozen-phonon approach produced significant amounts of imaginary phonon modes, as shown in Fig. 5a. In addition, we observed phonon softening, which cannot be described by conventional phonon approaches. This softening observation was attributed to the free molecular rotation, which reduces the “local” interaction between the “frozen” MA molecule and the PbBr<sub>3</sub> frame.

Based on the RT phonon dispersion, we calculated the IR absorption spectrum as shown in Fig. 4b. We found three main peaks at approximately 0.6, 1.2, and 1.8 THz, which match well with our experimental observations. The frozen-phonon approach was also applied to compute the IR spectrum, which shows a peak at a much higher frequency, as shown in Fig. 5b, for comparison. To understand the main origin of the three IR absorption peaks, we show the corresponding phonon vibrational modes in Fig. 4c–e. We found that the strong IR absorption peaks are mainly associated with the vibrational modes of the Pb–Br inorganic frame. The first and second peaks correspond to the transverse and longitudinal optical vibrations of the Pb–Br–Pb bonds, respectively, as shown in Fig. 4c, d. The optical Br vibration modes that are nearly normal to the Pb–Br–Pb bonds with stationary Pb atoms (Fig. 4e) lead to the third peak. The animation of all the vibrational modes contributing to the three IR peaks can be found in the Supplementary Information.

In conclusion, to explore the possibility of novel THz-based applications using OHP materials, we investigated

the phonon modes of MAPbBr<sub>3</sub> hybrid perovskite thin films on a PET flexible substrate with an ultrathin PTAA protective layer fabricated by the SVE method. We confirmed that there is no influence from defects such as C–O/Pb metal impurities and CH<sub>3</sub>NH<sub>2</sub> molecular defects on the THz-wave absorption property, which shows three fixed and stable absorptions at 0.8, 1.4, and 2.0 THz. The phonon modes from this study originated from the transverse vibration (0.8 THz), the longitudinal optical vibrations (1.4 THz) of the Pb–Br–Pb bonds, and the optical Br vibration (2.0 THz). We thus present this newly developed candidate organic–inorganic hybrid material for THz-based applications such as THz-wave sensing, modulation and imaging devices.

#### Acknowledgements

This work was supported by funding from the Faculty of Pure and Applied Sciences at the University of Tsukuba and JSPS KAKENHI Grant No. 17K05033 (Japan). This work was also supported by the Basic Science Research Program (NRF-2018R1D1A1B07047762, NRF-2020R1C1C1013646) through the National Research Foundation of Korea. We acknowledge the financial support from the Korean government through the National Research Foundation (2019R1A2C1005417). A portion of our computational work was done using the resources of the KISTI Supercomputing Center (KSC-2018-CHA-0052). This work was also supported by the Australia Research Council through its DECRA and DP programs. This work was also supported by the Programs for Professor of Special Appointment and Distinguished Visiting Professor (Eastern Scholar) at the Shanghai Institutions of Higher Learning and the Shanghai Rising-Star Program (Grant No. 19QA1403800). Myungkwan Song, who is a principal researcher at the Korea Institute of Materials Science, is appreciated for offering PET and PES flexible substrates.

#### Author details

<sup>1</sup>YUHS-KRIBB, Medical Convergence Research Institute, College of Medicine, Yonsei University, Seoul 03722, Republic of Korea. <sup>2</sup>Department of Physics, Kyung Hee University, Seoul 02447, Republic of Korea. <sup>3</sup>Division of Materials Science, Nara Institute of Science and Technology, Nara 630-0192, Japan. <sup>4</sup>School of Chemical Engineering and Australian Institute for Bioengineering and Nanotechnology (AIBN), University of Queensland, QLD 4027 QLD, Australia. <sup>5</sup>Materials Genome Institute, Shanghai University, 200444 Shanghai, China. <sup>6</sup>Division of Materials Science, Faculty of Pure and Applied Sciences, University of Tsukuba, Ibaraki 305-8577, Japan

#### Conflict of interest

The authors declare that they have no conflict of interest.

#### Publisher's note

Springer Nature remains neutral with regard to jurisdictional claims in published maps and institutional affiliations.

**Supplementary information** is available for this paper at <https://doi.org/10.1038/s41427-020-0235-6>.

Received: 12 April 2020 Revised: 28 May 2020 Accepted: 2 June 2020

Published online: 03 August 2020

#### References

- Green, M. A. & Bremner, S. P. Energy conversion approaches and materials for high-efficiency photovoltaics. *Nat. Mater.* **16**, 23–34 (2016).
- Heo, J. H. et al. Efficient inorganic-organic hybrid heterojunction solar cells containing perovskite compound and polymeric hole conductors. *Nat. Photonics* **7**, 486–491 (2013).
- Yoo, E. J., et al. Resistive switching behavior in organic-inorganic hybrid CH<sub>3</sub>NH<sub>3</sub>PbI<sub>3-x</sub>Cl<sub>x</sub> perovskite for resistive random access memory devices. *Adv. Mater.* **27**, 6170–6175 (2015).
- Grätzel, N.-G. P. M. & Miyasaka, T. *Organic-Inorganic Halide Perovskite Photovoltaics* (Springer, 2016). [https://doi.org/10.1007/978-3-319-35114-8\\_4](https://doi.org/10.1007/978-3-319-35114-8_4)
- Sun, J., et al. Organic/inorganic metal halide perovskite optoelectronic devices beyond solar cells. *Adv. Sci.* **5**, 1700780 (2018).
- Ono, L. K. & Qi, Y. Research progress on organic-inorganic halide perovskite materials and solar cells. *J. Phys. D: Appl. Phys.* **51**, 093001 (2018).
- Lee, Y. M., et al. Comprehensive understanding and controlling the defect structures: an effective approach for organic–inorganic hybrid perovskite-based solar-cell application. *Front. Energy Res.* **6**, <https://doi.org/10.3389/fenrg.2018.00128> (2018).
- Stranks, S. D. & Snaith, H. J. Metal-halide perovskites for photovoltaic and light-emitting devices. *Nat. Nanotechnol.* **10**, 391–402 (2015).
- Green, M. A. et al. Solar cell efficiency tables (version 45). *Prog. Photovolt.* **23**, 1–9 (2015).
- Green, M. A., Ho-Baillie, A. & Snaith, H. J. The emergence of perovskite solar cells. *Nat. Photonics* **8**, 506–514 (2014).
- Song, T. Bin et al. Perovskite solar cells: film formation and properties. *J. Mater. Chem. A* **3**, 9032–9050 (2015).
- Brenner, T. M., Egger, D. A., Kronik, L., Hodes, G. & Cahen, D. Hybrid organic–inorganic perovskites: Low-cost semiconductors with intriguing charge-transport properties. *Nat. Rev. Mater.* **1**, 1–16 (2016).
- Khenkin, M. V. et al. Consensus statement for stability assessment and reporting for perovskite photovoltaics based on ISOS procedures. *Nat. Energy* **5**, 35–49 (2020).
- Boyd, C. C., Cheacharoen, R., Leijtens, T. & McGehee, M. D. Understanding degradation mechanisms and improving stability of perovskite photovoltaics. *Chem. Rev.* **119**, 3418–3451 (2019).
- Saliba, M. Perovskite solar cells must come of age: developing aging standards is required for industrialization. *Science* **359**, 388–389 (2018).
- Kim, N. K., et al. Investigation of thermally induced degradation in CH<sub>3</sub>NH<sub>3</sub>PbI<sub>3</sub> Perovskite solar cells using in-situ synchrotron radiation analysis. *Sci. Rep.* **7**, 4645 (2017).
- Lee, Y. M. et al. Surface instability of Sn-based hybrid perovskite thin film, CH<sub>3</sub>NH<sub>3</sub>SnI<sub>3</sub>: the origin of its material instability. *J. Phys. Chem. Lett.* **9**, 2293–2297 (2018).
- Babayigit, A. et al. Assessing the toxicity of Pb-and Sn-based perovskite solar cells in model organism *Danio rerio*. *Sci. Rep.* **6**, 18721 (2016).
- Tong, S., Von Schirnding, Y. E. & Prapamontol, T. Environmental lead exposure: a public health problem of global dimensions. *Bull. World Health Organ.* **78**, 1068–1077 (2000).
- Wang, C., Ecker, B. R., Wei, H., Huang, J. & Gao, Y. Environmental surface stability of the MAPbBr<sub>3</sub> single crystal. *J. Phys. Chem. C* **122**, 3513–3522.
- Oranskaia, A., Yin, J., Bakr, O. M., Brédas, J.-L. & Mohammed, O. F. Halogen migration in hybrid perovskites: the organic cation matters. *J. Phys. Chem. Lett.* **9**, 5474–5480.
- Park, J. S., Kim, S., Xie, Z. & Walsh, A. Point defect engineering in thin-film solar cells. *Nat. Rev. Mater.* **3**, 194–210 (2018).
- Hutter, E. M. et al. Direct-indirect character of the bandgap in methylammonium lead iodide perovskite. *Nat. Mater.* **16**, 115–120 (2017).
- Lee, Y. M. et al. Significant THz-wave absorption property in mixed δ- And α-FAPbI<sub>3</sub> hybrid perovskite flexible thin film formed by sequential vacuum evaporation. *Appl. Phys. Express* **12**, 051003 (2019).
- Maeng, I. et al. Significant THz absorption in CH<sub>3</sub>NH<sub>2</sub> molecular defect-incorporated organic-inorganic hybrid perovskite thin film. *Sci. Rep.* **9**, 5811 (2019).
- Weller, M. T., Weber, O. J., Henry, P. F., Di Pumpo, A. M. & Hansen, T. C. Complete structure and cation orientation in the perovskite photovoltaic methylammonium lead iodide between 100 and 352 K. *Chem. Commun.* **51**, 4180–4183 (2015).
- La-O-Vorakiat, C. et al. Phonon mode transformation across the orthorhombic-tetragonal phase transition in a lead iodide perovskite CH<sub>3</sub>NH<sub>3</sub>PbI<sub>3</sub>: a terahertz time-domain spectroscopy approach. *J. Phys. Chem. Lett.* **7**, 1–6 (2015).
- Brivio, F. et al. Lattice dynamics and vibrational spectra of the orthorhombic, tetragonal, and cubic phases of methylammonium lead iodide. *Phys. Rev. B: Condens. Matter Mater. Phys.* **92**, 144308 (2015).
- Maeng, I. et al. Strong linear correlation between CH<sub>3</sub>NH<sub>2</sub> molecular defect and THz-Wave absorption in CH<sub>3</sub>NH<sub>3</sub>PbI<sub>3</sub> hybrid perovskite thin film. *Nanomaterials* **10**, 721 (2020).

30. Ho, L., Pepper, M. & Taday, P. Terahertz spectroscopy: signatures and fingerprints. *Nat. Photonics* **2**, 541–543 (2008).
31. Hashimshony, D. et al. Characterization of the electrical properties and thickness of thin epitaxial semiconductor layers by THz reflection spectroscopy. *J. Appl. Phys.* **90**, 5778–5781 (2001).
32. Jeon, T. I. & Grischkowsky, D. Characterization of optically dense, doped semiconductors by reflection THz time domain spectroscopy. *Appl. Phys. Lett.* **72**, 3032–3034 (1998).
33. Samoska, L. A. An overview of solid-state integrated circuit amplifiers in the submillimeter-wave and THz regime. *IEEE Trans. Terahertz Sci. Technol.* **1**, 9–24 (2011).
34. Burford, N. M. & El-Shenawee, M. O. Review of terahertz photoconductive antenna technology. *Opt. Eng.* **56**, 010901 (2017).
35. Jung, M. C. et al. Formation of CH<sub>3</sub>NH<sub>2</sub>-incorporated intermediate state in CH<sub>3</sub>NH<sub>3</sub>PbI<sub>3</sub> hybrid perovskite thin film formed by sequential vacuum evaporation. *Appl. Phys. Express* **12**, 015501 (2019).
36. Wagner, C. D., Riggs, W. M., Davis, L. E., Moulder, J. F. & Muilenberg, G. E. *Handbook of X-ray Photoelectron Spectroscopy: A Reference Book of Standard Spectra for Identification and Interpretation Of Xps Data—Catalog—UW-Madison Libraries* (Physical Electronics, Chanhassen, MN, 1995).
37. Kohn, W. & Sham, L. J. Self-consistent equations including exchange and correlation effects. *Phys. Rev.* **140**, A1133 (1965).
38. Kresse, G. & Furthmüller, J. Efficient iterative schemes for ab initio total-energy calculations using a plane-wave basis set. *Phys. Rev. B: Condens. Matter Mater. Phys.* **54**, 11169–11186 (1996).
39. Kresse, G. & Hafner, J. Ab initio molecular dynamics for liquid metals. *Phys. Rev. B* **47**, 558–561 (1993).
40. Blöchl, P. E. Projector augmented-wave method. *Phys. Rev. B* **50**, 17953–17979 (1994).
41. Joubert, D. From ultrasoft pseudopotentials to the projector augmented-wave method. *Phys. Rev. B: Condens. Matter Mater. Phys.* **59**, 1758–1775 (1999).
42. Perdew, J. P., Burke, K. & Ernzerhof, M. Generalized gradient approximation made simple. *Phys. Rev. Lett.* **77**, 3865–3868 (1996).
43. Grimme, S., Antony, J., Ehrlich, S. & Krieg, H. A consistent and accurate ab initio parametrization of density functional dispersion correction (DFT-D) for the 94 elements H-Pu. *J. Chem. Phys.* **132**, 154104 (2010).
44. Wang, Y. et al. Pressure-induced phase transformation, reversible amorphization, and anomalous visible light response in organolead bromide perovskite. *J. Am. Chem. Soc.* **137**, 11144–11149 (2015).
45. Hellman, O., Abrikosov, I. A. & Simak, S. I. Lattice dynamics of anharmonic solids from first principles. *Phys. Rev. B: Condens. Matter Mater. Phys.* **84**, 180301 (2011).
46. Hellman, O., Steneteg, P., Abrikosov, I. A. & Simak, S. I. Temperature dependent effective potential method for accurate free energy calculations of solids. *Phys. Rev. B: Condens. Matter Mater. Phys.* **87**, 104111 (2013).
47. Hellman, O. & Abrikosov, I. A. Temperature-dependent effective third-order interatomic force constants from first principles. *Phys. Rev. B: Condens. Matter Mater. Phys.* **88**, 144301 (2013).
48. Nosé, S. An extension of the canonical ensemble molecular dynamics method. *Mol. Phys.* **57**, 187–191 (1986).
49. Hoover, W. G. Canonical dynamics: equilibrium phase-space distributions. *Phys. Rev. A* **31**, 1695–1697 (1985).
50. Skelton, J. M. et al. Lattice dynamics of the tin sulphides SnS<sub>2</sub>, SnS and Sn<sub>2</sub>S<sub>3</sub>: vibrational spectra and thermal transport. *Phys. Chem. Chem. Phys.* **19**, 12452–12465 (2017).
51. Togo, A. & Tanaka, I. First principles phonon calculations in materials science. *Scr. Mater.* **108**, 1–5 (2015).
52. Wang, K. H., Li, L. C., Shellaiah, M. & Sun, K. W. Structural and photophysical properties of methylammonium lead tribromide (MAPbBr<sub>3</sub>) single crystals. *Sci. Rep.* **7**, 1–14 (2017).
53. Jung, M.-C. et al. Formation of CH<sub>3</sub>NH<sub>2</sub>-incorporated intermediate state in CH<sub>3</sub>NH<sub>3</sub>PbI<sub>3</sub> hybrid perovskite thin film formed by sequential vacuum evaporation. *Appl. Phys. Express* **12**, 015501–015501 (2018).
54. Jung, M.-C., et al. The presence of CH<sub>3</sub>NH<sub>2</sub> neutral species in organometal halide perovskite films. *Appl. Phys. Lett.* **108**, 073901 (2016).
55. Yi, Z. et al. Will organic-inorganic hybrid halide lead perovskites be eliminated from optoelectronic applications? *Nanoscale Adv.* **1**, 1276–1289 (2019).
56. Jung, M.-C. et al. Clean interface without any intermixed state between ultrathin P3 polymer and CH<sub>3</sub>NH<sub>3</sub>PbI<sub>3</sub> hybrid perovskite thin film. *Sci. Rep.* **9**, 1–6 (2019).
57. Sendner, M. et al. Optical phonons in methylammonium lead halide perovskites and implications for charge transport. *Mater. Horiz.* **3**, 613–620 (2016).
58. Zhao, D. et al. Low-frequency optical phonon modes and carrier mobility in the halide perovskite CH<sub>3</sub>NH<sub>3</sub>PbBr<sub>3</sub> using terahertz time-domain spectroscopy. *Appl. Phys. Lett.* **111**, 201903 (2017).